Chinese Journal of Chemical Engineering 94 (2026) 1–16

Contents lists available at ScienceDirect

Chinese Journal of Chemical Engineering

journal homepage: www.elsevier.com/locate/CJChE

Full Length Article

Experimental study of flow boiling characteristics of ethylene glycol/water mixtures in titanium narrow-gap microchannel under sub-atmospheric pressure

Dahai Wang [1], Xianan Yin [1], Chen Zhao [2], Qiushi Gu [3], Chaoyang Zhang [3,*]

[1] School of Carbon Neutrality Science and Engineering, Anhui University of Science and Technology, Hefei 230031, China
[2] School of Mechanical Engineering, Shanghai Jiao Tong University, Shanghai 200240, China
[3] Paris Elite Institute of Technology, Shanghai Jiao Tong University, Shanghai 200240, China

ARTICLE INFO

Article history:
Received 28 September 2025
Received in revised form
28 December 2025
Accepted 30 December 2025
Available online 28 January 2026

Keywords:
Flow
Bubble
Ethylene glycol/water mixtures
Two-phase flow
Narrow-gap channel
Sub-atmospheric pressure

ABSTRACT

Narrow-gap channels offer strong heat transfer capability and structural stability, making them suitable for high-heat-flux cooling in compact systems. This study experimentally investigates the boiling performance of a titanium narrow-gap channel under sub-atmospheric pressure using an ethylene glycol—water mixture with a mass concentration of 55%. The effects of channel height, surface condition, mass flux, inlet subcooling, and saturation temperature were systematically examined, and bubbly flow, slug flow, and micro-bubble emission boiling were observed. Channel height strongly influenced boiling behavior: the 1.0 mm and 0.5 mm channels achieved significantly higher heat transfer coefficients than the 2.0 mm channel, while the 0.5 mm channel exhibited a much larger pressure drop, making the 1.0 mm channel the most practical configuration. Surface oxidation was identified as a major degradation factor, altering wettability, reducing nucleation-site activity, and causing periodic boiling crises that sharply reduced performance. Increasing mass flux improved the average heat transfer coefficient by enhancing convection and bubble removal, although the nucleate boiling enhancement factor decreased from 1.66 to 1.30 as nucleation became suppressed. Reducing the inlet subcooling from 30 °C to 20 °C promoted earlier boiling and more vigorous vapor generation, increasing the heat transfer coefficient by 65%. These results clarify how geometric, surface, and thermal–hydraulic parameters jointly control boiling in titanium narrow-gap channels and provide guidance for designing high-heat-flux cooling systems.
© 2026 The Chemical Industry and Engineering Society of China, and Chemical Industry Press Co., Ltd. All rights are reserved, including those for text and data mining, AI training, and similar technologies.

1. Introduction

With the rapid advancement of technology, cooling systems capable of handling high heat flux densities have garnered significant attention from both academia and industry [1]. In the electronics industry, the continuous increase in computing chip processing power coupled with the reduction in device size has led to a sharp rise in heat generation per unit area. This trend has made thermal management a critical challenge that constrains further technological development [2]. Among various cooling methods, flow boiling heat transfer technology has emerged as a mainstream solution. For applications requiring heat flux densities exceeding 500 $W \cdot cm^{-2}$, narrow gap channels have proven to be a promising active cooling technology due to their high heat transfer efficiency, compact structure, and operational stability [3,4]. Despite its lower thermal conductivity compared with conventional heat-sink materials, titanium exhibits excellent high-temperature stability, corrosion resistance, and compatibility with extreme or vacuum environments (*e.g.*, plasma-facing collector structures), making it particularly suitable for narrow-gap cooling applications where structural reliability is critical. Studying titanium channels therefore provides valuable insight into how material properties influence bubble dynamics and boiling heat transfer under extreme conditions.

Research on two-phase flow and heat transfer in narrow gap channels has predominantly utilized deionized water as the working fluid, as demonstrated by studies conducted by Krishnan

* Corresponding author.
E-mail address: chaoyzhang@sjtu.edu.cn (C. Zhang).

https://doi.org/10.1016/j.cjche.2025.12.022
1004-9541/© 2026 The Chemical Industry and Engineering Society of China, and Chemical Industry Press Co., Ltd. All rights are reserved, including those for text and data mining, AI training, and similar technologies.

et al. [5], Alam *et al.* [6], Zhou *et al.* [4]. While deionized water is widely employed for its excellent thermal conductivity and high specific heat capacity, its freezing point limits its applicability in low-temperature environments. In contrast, ethylene glycol–water solutions, commonly used as antifreeze, can achieve freezing points below −40 °C at specific ratios. With thermal properties comparable to those of deionized water, these solutions are considered excellent alternatives for cooling applications in extreme conditions [7].

Recent studies have explored the boiling heat transfer performance of ethylene glycol–water solutions across various configurations, including stainless steel tubes, jets, rectangular channels, and fins. Hu *et al.* [8] investigated the subcooled flow boiling of a 50% volume concentration ethylene glycol–water solution in a horizontal rectangular channel, noting that the heat transfer coefficient (HTC) on aluminum surfaces exceeded that on cast iron surfaces due to differences in material thermal properties. They introduced a novel parameter to account for the influence of heated surface properties on boiling behavior and proposed a new predictive model. Yu *et al.* [7,9] studied the subcooled flow boiling heat transfer of a 50/50 ethylene glycol–water solution in stainless steel tubes and fined aluminum channels, identifying two distinct regions: single-phase heat transfer and subcooled boiling. Their results indicated that subcooled boiling enhanced HTC by 25% to 30% on smooth aluminum surfaces with limited nucleation sites. Lee *et al.* [10] examined the heat transfer characteristics of ethylene glycol–water solutions in a rectangular channel with small flat heaters, observing that nucleate boiling bubbles in these solutions were typically larger than those in water. However, increasing flow rates significantly suppressed nucleate boiling. Under low-pressure conditions, the wall superheat at the onset of nucleate boiling (ONB) decreased with increasing pressure, while the HTC in the nucleate boiling zone exhibited variations with heat flux. Because sub-atmospheric boiling involves distinct thermophysical and interfacial phenomena compared with atmospheric boiling, an overview of pressure effects is necessary to contextualize our study.

The impact of pressure on boiling heat transfer has been extensively studied in conventional-sized channels [11] and micro-sized channels [12] under atmospheric and high-pressure conditions. However, at atmospheric pressure, the boiling point of ethylene glycol–water solutions are 108.73 °C, making phase change difficult to achieve at low heat flux densities. To address this, engineers often reduce saturation pressure to lower the boiling point. Under sub-atmospheric system pressure (SSP), the latent heat of vaporization increases, while the saturation temperature and specific vapor volume decrease [13]. These changes can lead to larger bubble departure sizes, significantly affecting heat transfer characteristics. Das *et al.* [14] demonstrated that reducing the saturation pressure of FC-72 to 30–40 °C optimized heat transfer performance. Colgan's research [15] on distilled water under sub-atmospheric pressure conditions revealed that bubble departure sizes increased while departure frequencies decreased, with critical heat flux (CHF) diminishing as system pressure decreased. Yin *et al.* [16] found that under sub-atmospheric pressure, the HTC of R-134a was largely unaffected by mass flux, but increased subcooling enhanced heat transfer performance. Conversely, Chang's study [17] on FC-72 indicated that under sub-atmospheric pressure, increased subcooling reduced HTC, bubble departure diameter, and nucleation site density.

Given the distinct heat transfer phenomena and mechanisms under sub-atmospheric pressure compared to atmospheric and high-pressure conditions, there is a pressing need to study flow boiling in sub-atmospheric pressure environments. Such research has significant practical implications for applications such as high-altitude aircraft [18], lunar surface crew cabins [15], seawater desalination [19], and heat pipes [20]. Additionally, researchers have explored the use of nanoparticles to enhance the heat transfer capabilities of ethylene glycol–water solutions [21–24]. While nanofluids have shown potential in improving heat transfer performance, gravitational effects can compromise fluid stability, potentially damaging pump blades or clogging flow passages.

Despite the growing interest in ethylene glycol–water solutions as a working fluid for phase change heat transfer, research on their behavior under sub-atmospheric pressure remains limited. Bubble nucleation, dynamics, and CHF under these conditions differ significantly from those at atmospheric pressure, highlighting the need for further investigation. To address these gaps, this study conducts experimental research on the heat transfer characteristics of ethylene glycol–water solutions in narrow titanium channels under sub-atmospheric pressure conditions. The work comprehensively evaluates boiling curves and average HTCs, providing valuable insights for optimizing high heat flux cooling systems.

2. Experimental Setup and Data Reduction

2.1. Experiment loop

Fig. 1 shows the schematic of the narrow-gap flow boiling experimental setup, comprising a test section, preheater, liquid reservoir, gear pump, plate heat exchanger, and accumulator, connected in a counterclockwise loop with all components horizontally aligned. The stainless steel 304 liquid reservoir, located 20 cm above the main loop and downstream of the gear pump, enables fluid filling, pressure fluctuation damping, and removal of non-condensable gases. A plate heat exchanger (Wuxi Lehman, Jiangsu, China) cools the test section outlet fluid to a set temperature before reheating in the preheater to the desired inlet condition. The outlet pressure is controlled *via* a vacuum pump connected to the accumulator gas side.

To establish and maintain sub-atmospheric conditions, the entire two-phase loop was first evacuated and subjected to a vacuum leak test, as negative-pressure operation requires stricter sealing than conventional positive-pressure nitrogen testing. After confirming leak-tightness, non-condensable gases were removed by filling the elevated reservoir with the ethylene glycol–water solution, evacuating the remaining components, and circulating the fluid so that residual gases migrated to the reservoir and were displaced. System pressure was then controlled using an accumulator equipped with a deformable rubber bladder: evacuating or admitting gas on the bladder side adjusted the liquid-side pressure and corresponding saturation temperature. Pressure was monitored continuously through the data acquisition system, enabling fine control to maintain stable sub-atmospheric boiling conditions throughout the experiments.

The working fluid (ethylene glycol–water solution with a mass concentration of 55%, volume concentration of 52.7%, freezing point −43.6 °C, boiling point 108.3 °C at 100 kPa) is driven by a gear pump (Micropump-GB, USA) through a mass flow meter (Bronkhorst M15-AGD-99-0-S, Netherlands), preheated to the target inlet temperature, and heated in the test section to induce liquid–vapor phase change. The two-phase mixture is subsequently cooled in the plate heat exchanger by a constant-temperature water loop and returned to the pump. Flow rate is adjusted by varying the DC motor voltage, while inlet temperature is controlled by regulating the constant-temperature bath and preheater power. T-type armored thermocouples and pressure transducers (GE-PMP5075, China) installed upstream and downstream of the test section to measure inlet/outlet temperatures

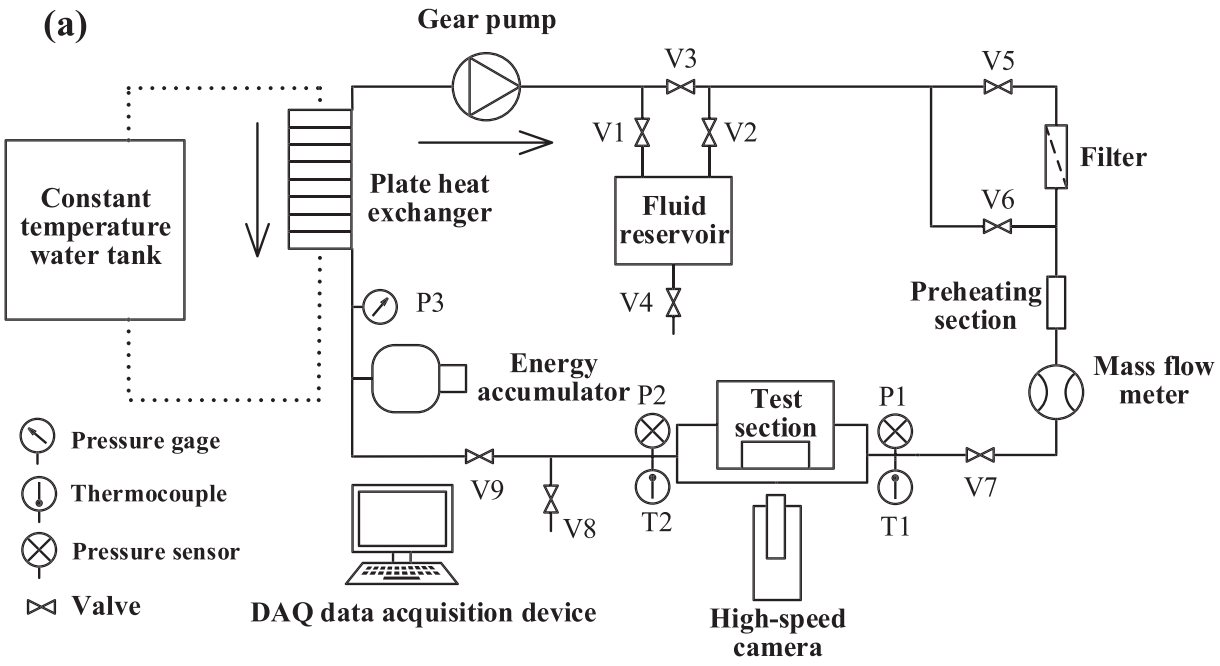


Fig. 1. Experimental system: (a) schematic of the test facility, (b) experimental installation of test section.

and pressures, with all signals recorded *via* a data acquisition system. Under test conditions, the back pressure is maintained at (51.9 ± 0.5) kPa, yielding a boiling point of (90 ± 0.3) °C and a latent heat of 2602.165 kJ·kg^{-1}.

2.2. Test section

The test section consists of a narrow-gap channel and a heating module, as illustrated in Fig. 2. The titanium alloy flow channel is fastened onto the heating module with bolts, with TP-II thermal interface material (TIM) inserted between them to reduce contact thermal resistance. In the heating module, heat is supplied by six cartridge heaters embedded in a copper heat collector block (maximum power 150 W each, rated up to 1000 °C). The heater output is controlled by adjusting the DC power supply voltage. Mica insulation is placed around the copper block, while the thermocouple outlet windows are sealed with glass to minimize infrared radiation losses. The entire heating module is wrapped with asbestos and thermal foam to further reduce heat loss. Twelve thermocouples (six on each side of the copper block) are used to measure the internal temperatures for heat flux calculation, and two additional thermocouples near the heaters monitor the copper block temperature to prevent overheating and heater damage. The titanium alloy channel assembly comprises an

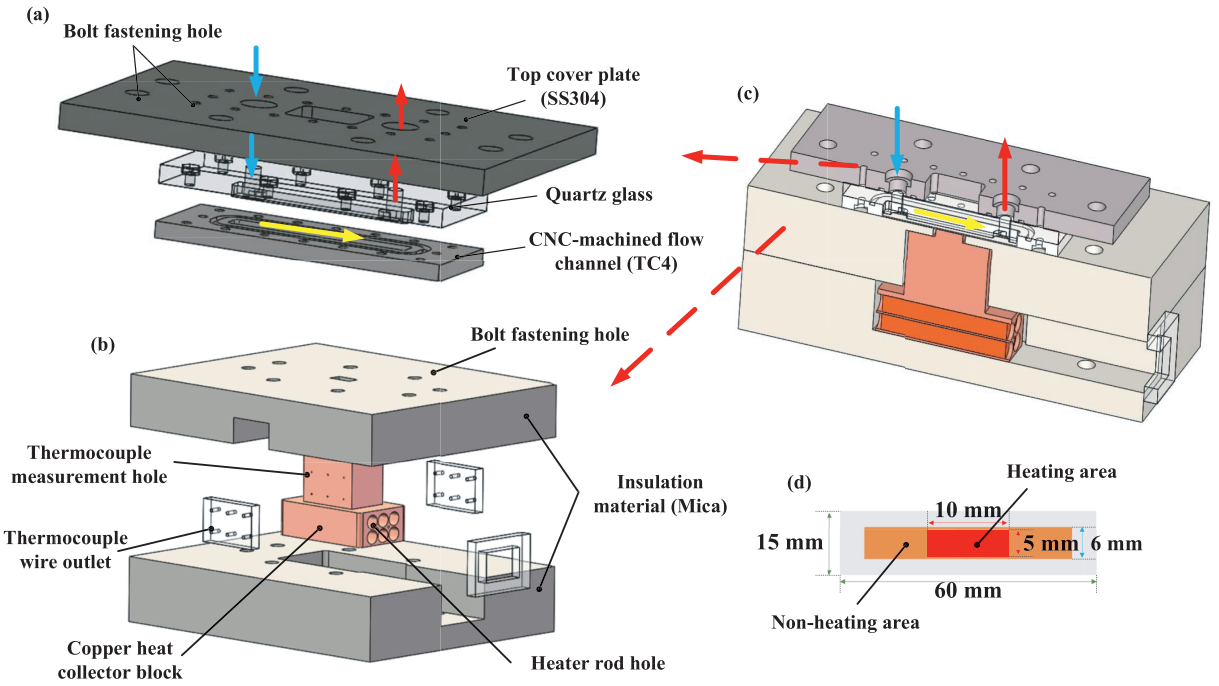


Fig. 2. Schematic diagrams of test section and heating block: (a) a titanium alloy integrated processing runner; (b) heating model; (c) overall 3-D profile diagram of test section; (d) flow channel heating area.

integrated flow channel, a quartz glass viewing window, and a stainless-steel top cover plate. The integrated flow channel is CNC-machined. Due to the low thermal conductivity of titanium (Table 1), even with a wall thickness of 400 μm, a surface temperature exceeding 100 °C is observed between the top and bottom surfaces under a heat flux of 250 W·cm^{-2}. The quartz glass viewing window is laser-cut for precision and, when assembled with the titanium flow channel, forms a 1 mm-high narrow-gap channel. All joints are sealed with nitrile O-rings and secured with bolts.

Because the titanium channel wall is too thin to embed thermocouples, its surface temperature is calculated using Fourier's law of heat conduction while neglecting lateral heat losses. Numerical simulations confirm that, for a 400 μm thick titanium wall, the temperature distribution is concentrated in the region in contact with the copper block and closely matches the Fourier-based calculation, while at the boundaries the temperature drops sharply to ambient due to large gradients.

The titanium channel has a total length of 60 mm and width of 15 mm, with a flow channel section measuring 50 mm × 6 mm. The heating area is centered, with dimensions of 10 mm × 5 mm. Upstream and downstream of the heating area, two 20 mm-long buffer zones are included to minimize the effect of perpendicular fluid entry and to ensure uniform fluid mixing.

To ensure safe loop operation and achieve the required inlet water temperature, a preheating section was incorporated between the gear pump and the test section. This modification addresses two operational constraints: (1) When the water pump of the constant-temperature bath operates at its maximum allowable temperature, the cooling water cannot achieve the desired inlet temperature. (2) Reducing the cooling capacity to raise the temperature which risks cavitation in the gear pump, posing safety hazards to the loop. The preheating section heats the working fluid exiting the gear pump to the target experimental inlet temperature. Its structure is shown in Fig. 3. The preheater consists of two main components: the flow channel and the heating module. The flow channel assembly comprises an aluminum-alloy channel body, copper heat transfer fins, and an aluminum-alloy top cover plate. The heating module includes mica insulation, a primary copper block, and a secondary copper block. All components are fastened with bolts and sealed with nitrile O-rings.

Heat is conducted from the primary copper block to the secondary copper block, where it is collected and transferred to the heat transfer fins. The top surface of the heating block measures 45 mm × 45 mm to reduce local heat flux and avoid exceeding the CHF. Thermal grease is applied to the heating block's top surface to ensure intimate contact with the preheater's bottom surface, thereby minimizing contact thermal resistance. Additionally, temperature monitoring points are embedded within the secondary copper block to track temperature variations in real time, preventing overheating of the heating block and ensuring the thermal grease operates within its allowable temperature range for optimal heat transfer performance.

2.3. Data reduction

In the design of the experimental system, the heating copper block of the test section was surrounded by mica, asbestos, and thermal insulation foam to minimize heat losses to the surroundings, thereby providing a basis for subsequent thermal analysis. Assuming negligible heat loss, the temperature field within the heating copper block can be approximated as a one-dimensional steady-state heat conduction problem. The average heat flux is calculated using Fourier's law as:

$$q = 12 \times \lambda_{T2} \times \frac{1}{a} \sum_{i=1}^{a} (t_{1-i} - t_{2-i}) / \Delta z \tag{1}$$

As shown in Fig. 4, t_{2-i} represents the temperature readings from the six thermocouples in the upper layer, and t_{1-i} represents those from the six thermocouples in the lower layer. The distance between the two thermocouple layers is $\Delta z = 10$ mm, and λ_{T2} is the

Table 1
Thermal conductivity of TC4.

Temperature, T/°C	Thermal diffusivity, α/mm$^2\cdot$s^{-1}	Specific heat capacity, C_p/J$\cdot$g$^{-1}\cdot$K^{-1}	Thermal conductivity, λ_{TC4}/W$\cdot$m$^{-1}\cdot$K^{-1}
25.2	2.869	2.444	7.014
100.0	3.072	2.564	7.878
200.0	3.349	2.589	8.699
300.0	3.622	2.746	10.057
400.0	3.954	2.842	11.235
500.0	4.237	3.071	13.012

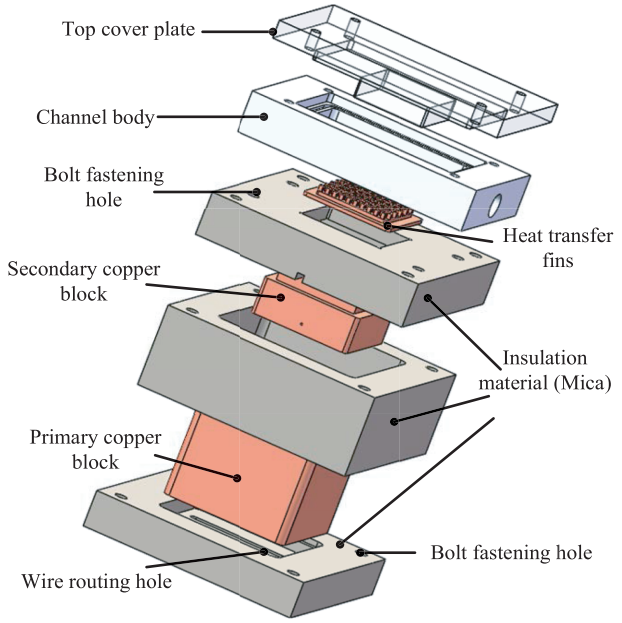


Fig. 3. Schematic of preheating section.

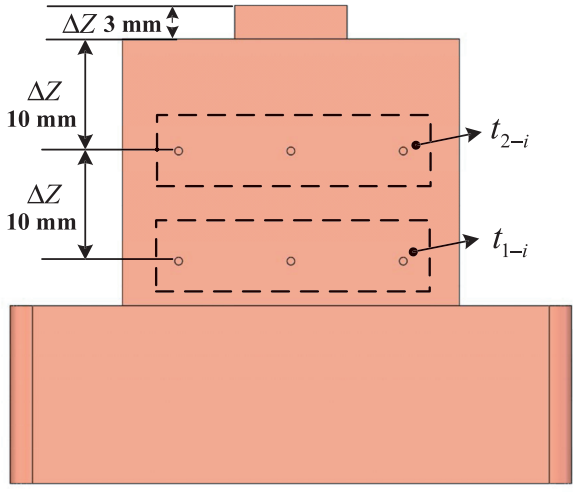


Fig. 4. Schematic diagram of the heat collecting copper block in the experimental section.

thermal conductivity of the heating copper block (copper), calculated as:

$$\lambda_{T2} = -0.0644 \times T + 382.87 \tag{2}$$

where T is copper block temperature (°C). The interface between the copper block and the titanium plate is filled with TP-II TIM, whose thermal conductivity is fixed at 80 W$\cdot$m$^{-1}\cdot$K^{-1}.

The titanium narrow-gap channel (TNGC), with a thickness of only 400 μm, cannot accommodate thermocouples to directly measure the bottom surface temperature T_{int}. The wall surface temperature of the narrow-gap channel (T_{surf}) is therefore calculated using the following equations:

$$T_{Cu} = \frac{-b_{T2} + \sqrt{(k_{T2} \times T_{2-i} + b_{T2})^2 - 2 \times k_{T2} \times \frac{q}{12} \times \Delta z}}{k_{T2}} \tag{3}$$

$$T_{down} = \frac{-b_{T2} + \sqrt{(k_{T2} \times T_{Cu} + b_{T2})^2 - 2 \times k_{T2} \times q \times \Delta z}}{k_{T2}} \tag{4}$$

$$T_{surf} = \frac{-b_{TC4} + \sqrt{(k_{TC4} \times T_{down} + b_{TC4})^2 - 2 \times k_{TC4} \times q \times \Delta z}}{k_{TC4}} \tag{5}$$

Here, $k_{T2} = -0.0644$, $b_{T2} = 382.87$, $k_{TC4} = 0.0123$, and $b_{TC4} = 6.5142$. In Eqs. (3)–(5), T_{Cu} and T_{down} are intermediate variables artificially defined to simplify the calculation process and have no direct physical meaning.

The average heat transfer coefficient h (representing the overall heat transfer capability of the narrow-gap channel) and the two-phase heat transfer coefficient h_{tp} (representing the two-phase heat transfer capability of the narrow-gap channel) are adopted as performance evaluation parameters:

$$h = \frac{q}{\left(T_{surf} - T_{in}\right)} \tag{6}$$

$$h_{tp} = \frac{q}{\left(T_{surf} - T_{sat}\right)} \tag{7}$$

To describe the operating conditions, the inlet subcooling of the working fluid (T_{sub}), the wall superheat (T_{sup}), and the mass flux (G) are defined as follows:

$$T_{sub} = T_{sat} - T_{in} \tag{8}$$

$$T_{sup} = T_{surf} - T_{sat} \tag{9}$$

$$G = \frac{\dot{m}}{A} \tag{10}$$

where T_{sat} is the saturation temperature (°C), T_{in} is the inlet temperature (°C), T_{surf} is the wall surface temperature (°C), $\dot{m}$ is the mass flux (kg$\cdot$s^{-1}), and A is the projected cross-sectional area of the narrow-gap channel perpendicular to the flow direction (m^2).

2.4. Uncertainty analysis

Experimental uncertainties include direct measurement errors (mass flux, pressure, and temperature) and indirect errors (heat flux). The direct errors are determined by the accuracy of the measurement instruments, while the indirect errors are evaluated using the error propagation method proposed by Moffat [25]:

$$U_R = \left[\sum_{i=1}^{n}\left(\frac{\partial R}{\partial X_i}\delta X_i\right)^2\right]^{\frac{1}{2}} \Big/ R \tag{11}$$

where U_R is the absolute uncertainty of parameter R, X_i represents the independent variables of R, and δX_i is the absolute uncertainty of X_i. The uncertainties of several physical quantities in this study are summarized in Table 2.

3. Results and Discussion

3.1. Comparison of heat transfer performance between ethylene glycol/water mixture and water

In this study, the term ethylene glycol solution specifically refers to an ethylene glycol–water mixture with a mass concentration of 55%. At this concentration, the mixture exhibits the lowest freezing point, enabling broader application potential. The mass concentration of ethylene glycol strongly influences its heat transfer performance because the thermophysical properties of binary mixtures vary significantly with concentration. Similar findings were reported by Lin *et al.* [26] in their investigation of methanol heat exchange performance, where mass flux and mass fraction were identified as the dominant parameters affecting boiling heat transfer. A methanol solution with a mass concentration of 30% exhibited optimal heat transfer performance and the highest CHF, largely due to the Marangoni effect on liquid film rupture. Although it is important to examine the heat transfer performance of ethylene glycol–water mixtures over a range of concentrations, such an analysis is beyond the scope of the present work. Unless otherwise stated, the term ethylene glycol solution hereafter refers to the mixture with a mass concentration of 55%.

As shown in Fig. 5, the ethylene glycol solution and deionized water differ markedly in thermophysical properties. The viscosity of the ethylene glycol solution decreases significantly with increasing temperature but remains substantially higher than that of deionized water. Although it increases slightly with temperature, the thermal conductivity of the ethylene glycol solution is only about 60% of that of deionized water. The specific heat capacity is comparable to that of deionized water but exhibits greater temperature dependence. These differences strongly influence both heat transfer performance and flow pressure drop.

Fig. 6 compares the heat transfer performance of a TNGC using either the ethylene glycol solution or deionized water as the working fluid, at an inlet temperature of 30 °C and under atmospheric pressure. The results agree with expectations based on thermophysical property differences: deionized water exhibits significantly higher heat transfer capability. The performance gap narrows with increasing mass flux, but remains substantial overall. Moreover, Fig. 6 shows that in the single-phase region, the influence of mass flux on performance differences is more pronounced than in the two-phase boiling region. Overall, the heat transfer capability of the ethylene glycol solution is approximately 60% that of deionized water.

Table 2
Overview of the experimental uncertainty of the experimental setup.

Parameter	Operating range	Uncertainties
Mass flux, $\dot{m}$/g·s^{-1}	6–18	±1%
Outlet pressure, P_{sat}/kPa	35.2–51.9	±0.5
Saturation temperature, T_{sat}/°C	80–90	±0.35
Inlet temperature, T_{in}/°C	55–65	±0.5
Wall surface temperature, T_{surf}/°C	73.7–152.1	±(1.86%–7.82%)
Heat flux, q/W·cm^{-2}	13.4–271.7	±(1.40%–13.74%)
Average heat transfer coefficient, h/kW·m^{-2}·K^{-1}	10.6–43.7	±(11.17%–23.93%)

3.2. Selection of channel height

In flow boiling research, channel height is recognized as a critical geometric parameter with a pronounced impact on heat transfer performance. Reducing the channel height can promote bubble nucleation and departure, thereby enhancing the HTC [27,28]. However, excessively small channel heights may adversely affect heat transfer performance, particularly by reducing the CHF [29,30]. This suggests the existence of a theoretical optimum channel height that maximizes heat transfer efficiency while avoiding adverse effects.

Fig. 7 presents the heat transfer performance of narrow-gap channels with different heights. The 0.5 mm and 1 mm channels exhibit comparable heat transfer characteristics. At low heat fluxes, the 0.5 mm channel outperforms the 1 mm channel, whereas at high heat fluxes their performance curves nearly coincide, which deviates slightly from the general conclusion noted above. This discrepancy is attributed to the suppression of the MEB phenomenon in excessively narrow channels, which reduces bubble-induced disturbance downstream and thus diminishes heat transfer enhancement.

Fig. 8 shows the pressure drop for three different channel heights. As channel height increases, the pressure drops decreases. The 0.5 mm channel exhibits a much higher pressure drop than the 1 mm and 2 mm channels; therefore, the 0.5 mm channel was excluded from systematic investigation in this work. The 2 mm channel demonstrates the lowest pressure drop but poor heat transfer performance, achieving only about 40% of the HTC of the 1 mm channel. Based on these results, a channel height of 1 mm was selected for the experimental investigations in this study.

A comparative evaluation of the three channel heights shows that the 0.5 mm and 1.0 mm channels provide substantially higher HTCs than the 2.0 mm channel, with the 1.0 mm channel achieving 80% to 90% of the enhancement obtained in the 0.5 mm channel. However, the hydraulic penalty differs significantly: the 0.5 mm channel exhibits a pressure drop 2–3 times higher than that of the 1.0 mm channel at similar mass flux. When considering the combined thermal–hydraulic performance (HTC/ΔP), the 1.0 mm channel consistently demonstrates the highest overall efficiency across the tested conditions. Thus, it offers the most practical balance between heat transfer enhancement and pumping-power requirements, making it the optimal choice for engineering applications.

3.3. Dynamics of flow boiling bubbles and micro-bubble emission boiling

Fig. 9 presents time-sequence visualization images of nucleate boiling of the ethylene glycol–water solution in the TNGC. A notable feature of narrow-gap channels is the large velocity gradient in the flow's vertical direction. Consequently, the two-phase flow regimes are dominated by bubbly flow and slug flow, with vigorous nucleate boiling as the primary mode, and occasional formation of relatively large bubbles at high heat fluxes. As

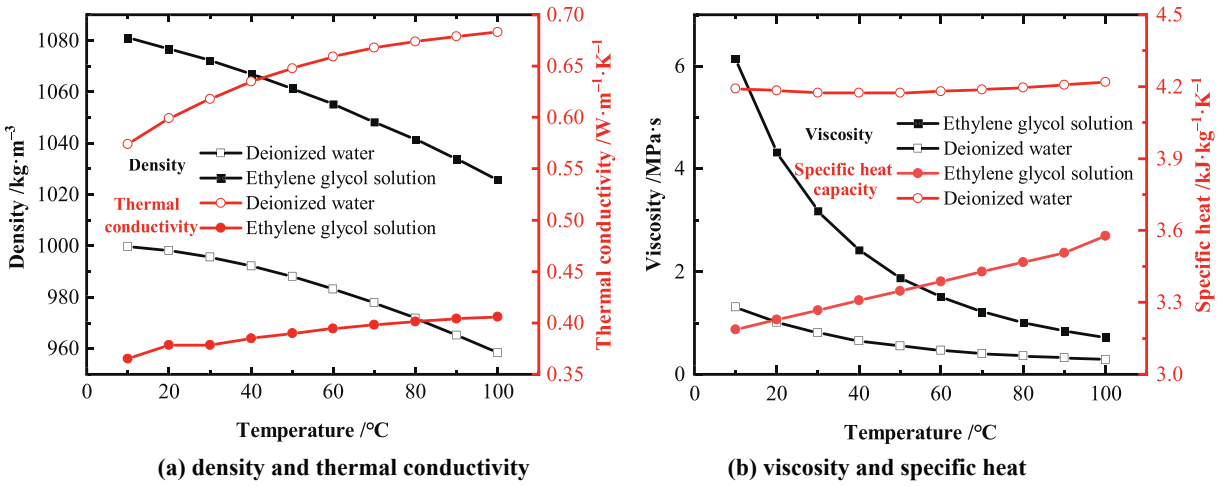


Fig. 5. Comparisons of thermal properties between deionized water and ethylene glycol solution.

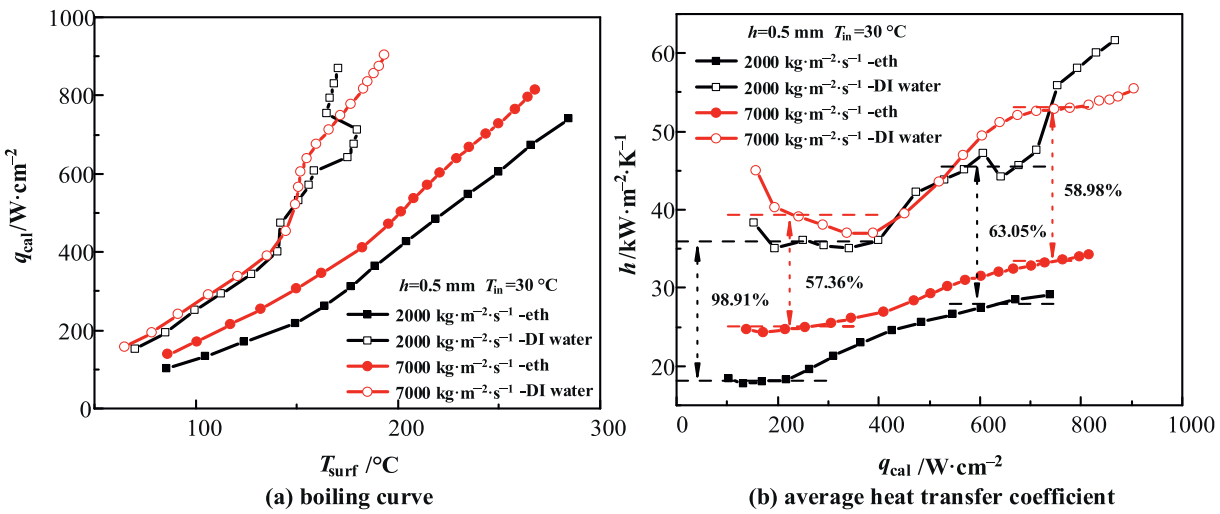


Fig. 6. Differences of heat transfer capacity between deionized water and ethylene glycol aqueous solution.

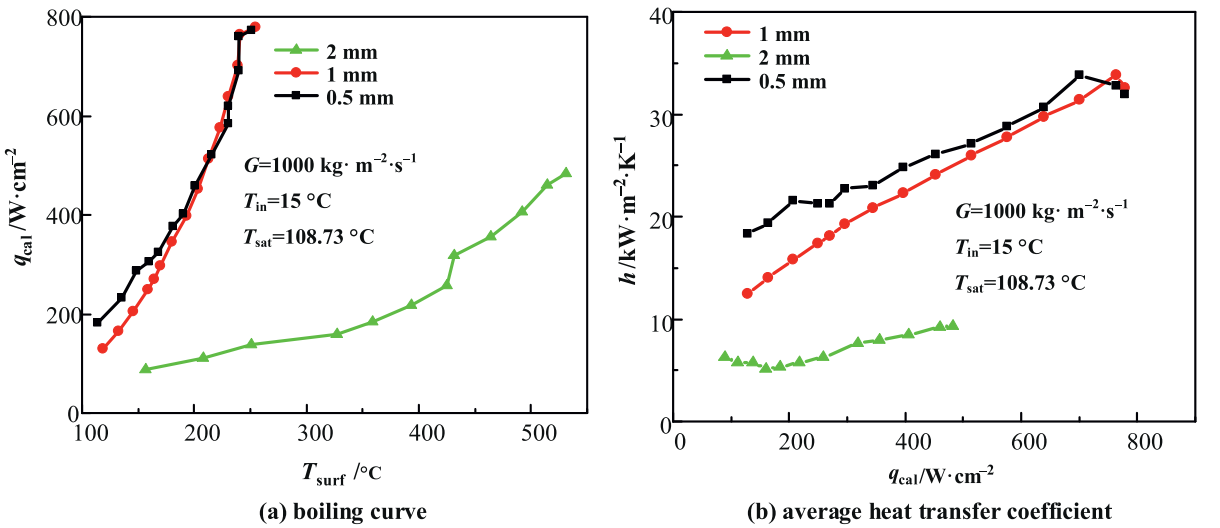


Fig. 7. Comparisons of heat transfer performance of narrow-gap channels with different heights.

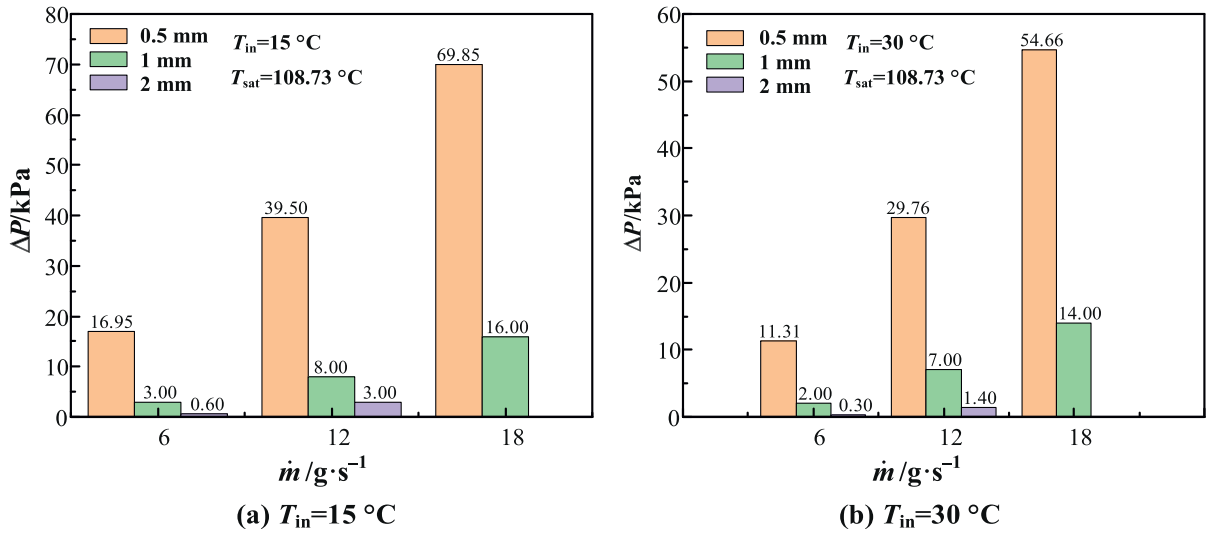


Fig. 8. Comparisons of pressure drop in different flow channels.

shown in Fig. 9, once the ONB is reached, phase change occurs at active nucleation sites, generating fine bubbles. The thin liquid microlayer surrounding these bubbles evaporates rapidly, causing the bubbles to grow in volume and move downstream with the bulk flow.

During this motion, some bubbles coalesce with those originating from other nucleation sites, forming larger bubbles, as illustrated in Fig. 10. When a bubble grows to a certain size, it detaches from the wall under the combined effects of lift forces and bulk fluid flow, entering the mainstream. A portion of these detached bubbles is cooled by the bulk liquid (*e.g.*, the bubble in Fig. 9 at 0.3 ms, which shrinks upon entering the mainstream), resembling a combination of nucleate boiling and MEB. The remaining bubbles are carried away directly by the bulk flow.

Fig. 11 illustrates the bubble flow characteristics during MEB at a heat flux of 502.1 W·cm^{-2}, flow velocity of 2 m·s^{-1}, and inlet temperature of 30 °C. During MEB, bubble nucleation occurs not only on the wall surface but also within the overheated downstream liquid. Wall nucleation is readily explained by the presence of active nucleation sites, which, once the heat flux is sufficient to activate them, generate bubbles periodically. When larger bubbles detach from the wall and are swept into the flow, part of them condenses upon contacting the cooler upper liquid, shrinking in size before disappearing, while others rupture during their ascent, producing numerous small bubbles. These small bubbles induce substantial fluid disturbance, thereby enhancing the heat transfer coefficient. Carried downstream by the flow, they serve as new nucleation sites; upon encountering hot fluid downstream, their volume increases again, forming new large bubbles. Experimental observations indicate that bubbles formed by the breakup of large bubbles generally do not reach the detachment size of wall-nucleated bubbles; although they grow in size, they remain significantly smaller than bubbles generated directly at the wall.

3.4. Impact of surface oxidation

Ethylene glycol is a chemically active substance prone to polymerization into high-molecular-weight polymers and further oxidative polymerization into organic acids. Due to the presence of hydroxyl groups, ethylene glycol readily reacts with dissolved oxygen in the system to form formic acid and oxalic acid. In preliminary experiments (surface temperature >300 °C), discoloration of the ethylene glycol–water solution was observed inside the tubing after repeated tests, which is likely caused by the combined effects of ethylene glycol decomposition at high temperature and the formation of various byproducts.

To investigate the decomposition rate of ethylene glycol under high-temperature conditions (>300 °C), gas chromatography–mass spectrometry (GC-MS) was employed to analyze the composition of the ethylene glycol–water solution after 20 days of high-temperature operation. Prior to analysis, the samples were extracted, and the extract was injected into the GC-MS. By comparing the peak areas with those of fresh ethylene glycol solution, it was determined that the ethylene glycol content decreased to only 76.6% of its initial value after 20 days (Table 3). Assuming a constant decomposition rate, the daily decomposition rate was approximately 1.16%. Analysis of the decomposition product peaks revealed the types and relative contents of major products: 1,2-propanediol (29.36%), 2-[2-[2-(2-hydroxyethoxy) ethoxy] ethoxy] ethanol (26.26%), and ethanol (17.64%), with other products at lower concentrations. These results indicate that, under high-temperature conditions, the ethylene glycol–water solution undergoes slow but continuous oxidative decomposition, producing various small organic molecules that may affect the chemical stability and thermophysical properties of the solution, and consequently its heat transfer performance.

In addition to the oxidation of ethylene glycol solution, metallic surfaces such as copper and titanium, due to their strong reducing ability, are also prone to oxidation under high-temperature conditions through reactions with dissolved oxygen, CO_2, and other species in water. This oxidation can significantly impact heat transfer performance, particularly when ethylene glycol–water solutions are used as specialized coolant media. The influence of oxidation on surface boiling heat transfer performance has not been extensively studied, with only a few researchers addressing this area. For example, Seong *et al.* [31] investigated the effect of surface oxidation on Zircaloy-4 and found that the formation of an oxide layer increased the nucleation site density, reduced bubble size, and improved CHF, attributed to additional nucleation sites from microcracks in the oxide layer and enhanced surface capillary wicking. Conversely, Jayaramu *et al.* [32] examined oxidation effects in copper channels and observed that, over time, the two-

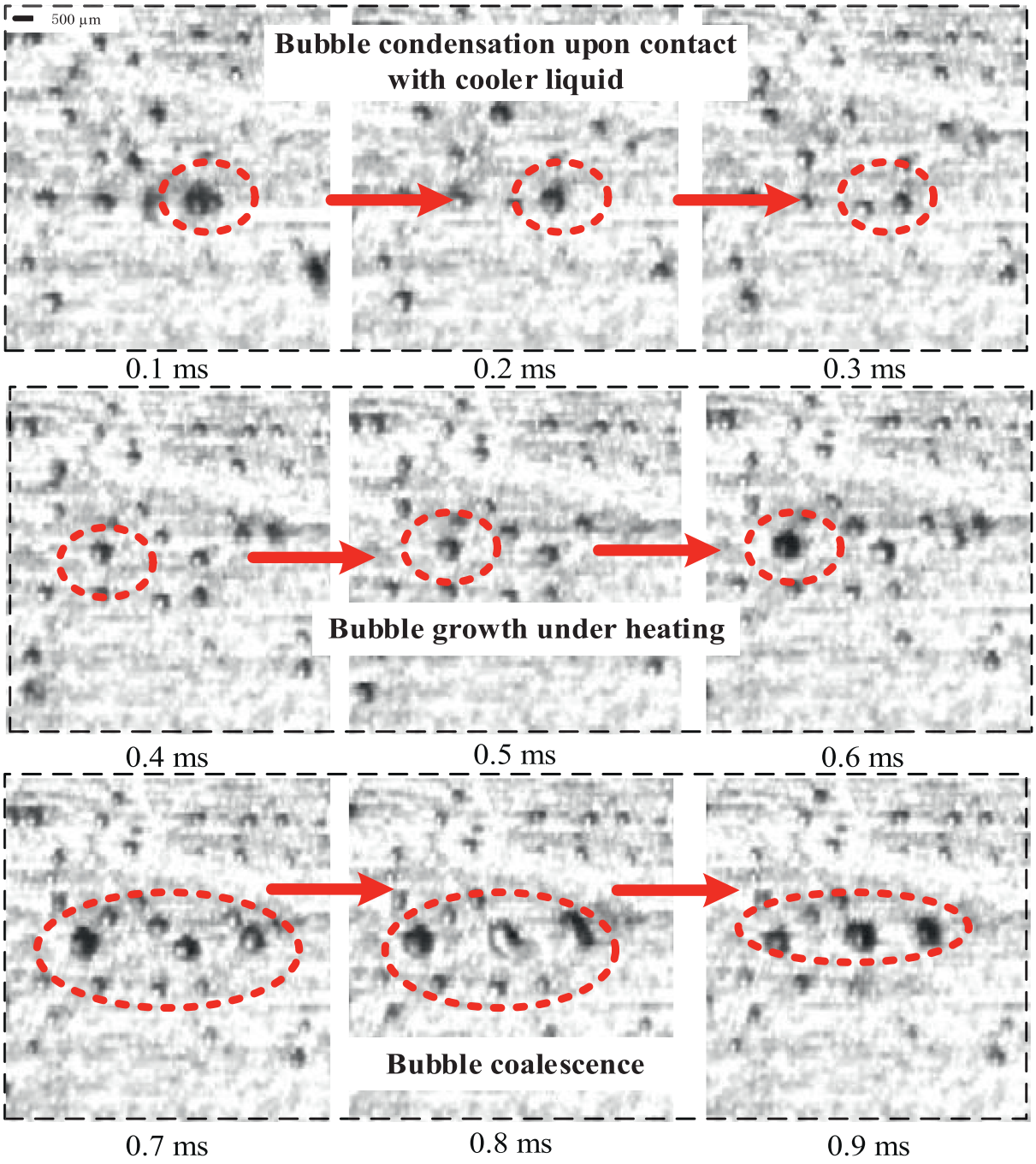


Fig. 9. Bubble development diagrams of nuclear boiling. The observation window (3 mm × 2.5 mm) is located at the center of the channel.

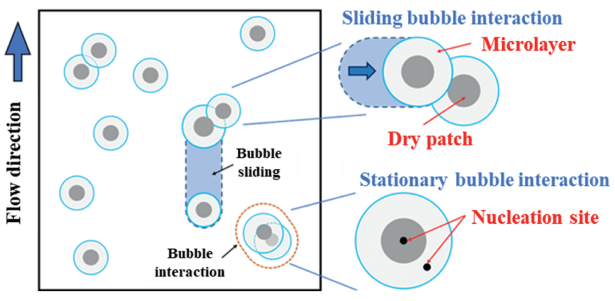


Fig. 10. Schematic diagram of nuclear boiling.

phase heat transfer coefficient decreased to about 60% of the unoxidized surface value and stabilized, while the two-phase pressure drops increased by approximately 13% [33], with no significant change in CHF. These changes were related to variations in surface wettability, consistent with observations by Wang *et al.* [34] and Wang and Dhir [35].

Fig. 12 compares the heat transfer performance of cleaned and uncleaned surfaces. Here, the cleaned surface refers to a post-test sample whose darkened oxide layer was removed by ultrasonic cleaning in citric acid, while the uncleaned surface refers to the darkened surface after testing without any treatment. Young *et al.* [36] reported oxide layer thicknesses of approximately

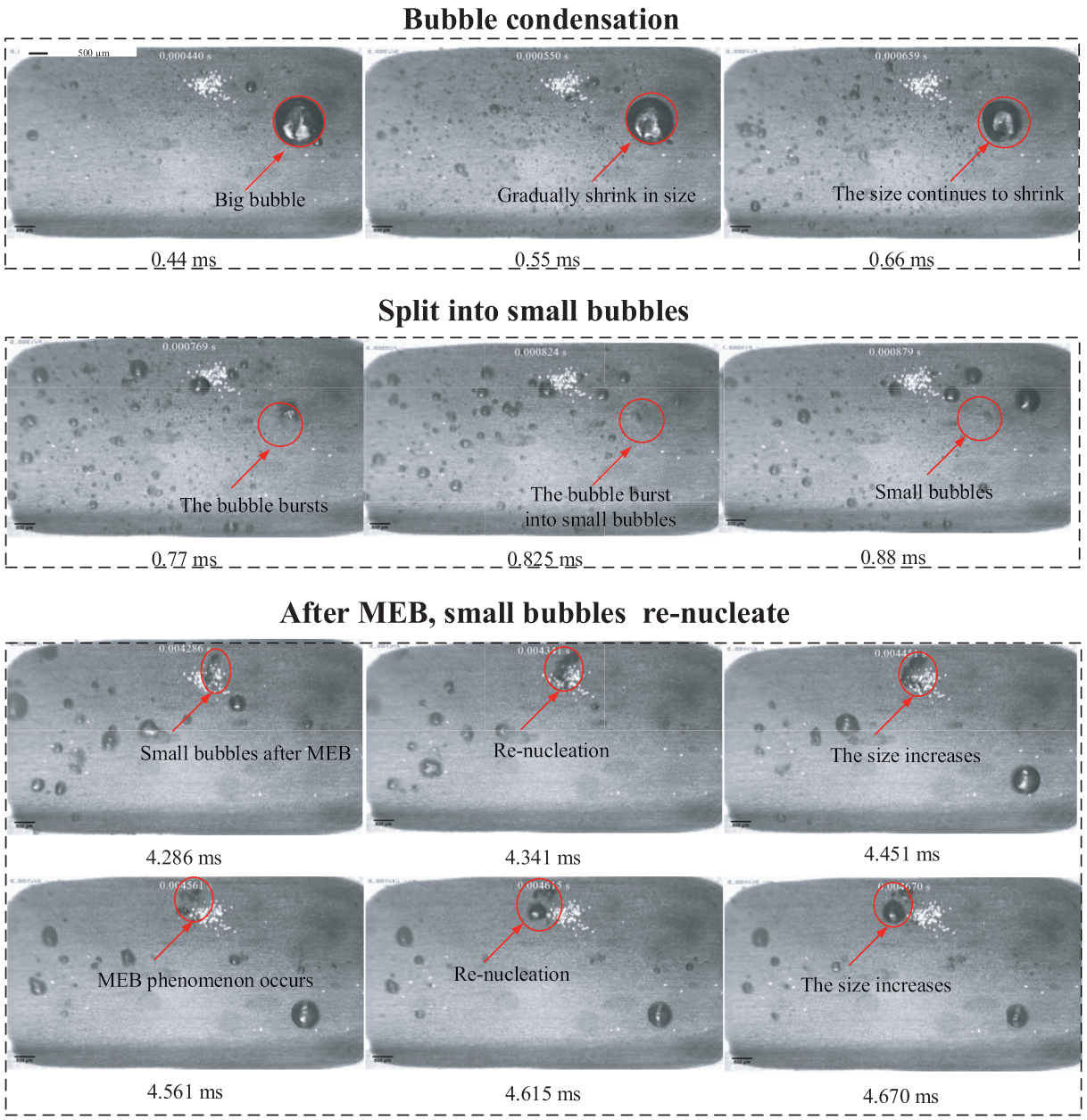


Fig. 11. Bubble development diagrams of MEB phenomenon. The observation window (3 mm × 6 mm) is located at the center of the channel.

Table 3
Comparison of peak area between two ethylene glycol solutions.

Sample type	Peak area/mAU·s	Match quality/%
Ethylene glycol–water solution	147724218	99.8
Ethylene glycol–water solution after 20 days of operation	113160388	100

90–300 nm and concluded that the observed reduction in heat transfer performance was not caused by a decrease in the thermal conductivity of the channel surface. Given the thinness of the oxide layer, its exact composition could not be determined; however, since it could be removed by citric acid, it is inferred to be an oxide.

From Fig. 12, the influence of surface oxidation is seen mainly in the two-phase region, especially at higher heat fluxes, whereas in the single-phase region and the early boiling development stage with sparse bubbles (heat flux < 400 $W \cdot cm^{-2}$), the curves nearly overlap. This suggests that oxidation has negligible influence on single-phase heat transfer and low-intensity nucleate boiling, which differs from Jayaramu's [32] findings and implies that the effects of oxidation on titanium and copper are not identical. When the heat flux exceeds 400 $W \cdot cm^{-2}$, the heat transfer capacity of the uncleaned surface decreases sharply, manifested by a

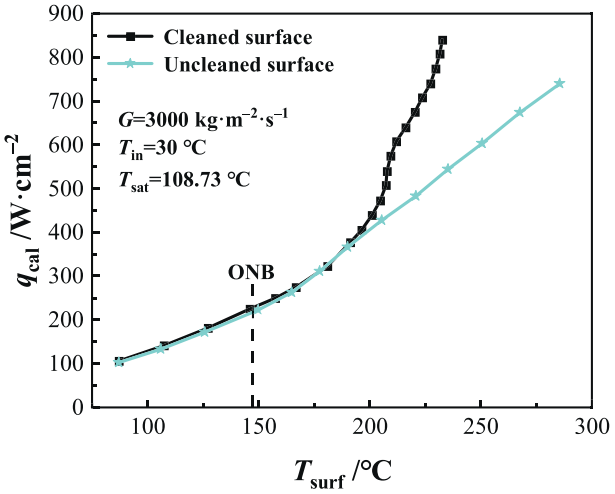


Fig. 12. Comparisons of heat transfer capacity between cleaned and uncleaned surfaces.

rightward shift of the boiling curve and a reduction in the average heat transfer coefficient *h*, indicating a change in boiling characteristics at high heat flux. At 740 W·cm^{-2} the cleaned surface maintains stable nucleate boiling, whereas the uncleaned surface exhibits periodic explosive boiling with a cycle of approximately 1.5 ms, clearly demonstrating the significant impact of surface oxidation on boiling heat transfer performance and bubble dynamics.

The occurrence of these phenomena on oxidized surfaces is consistent with expectations. Oxidation markedly increases surface wettability, reducing the liquid contact angle and enhancing liquid absorption capacity [31]. This change allows the ethylene glycol–water solution to more effectively wet and fill surface micropores and cavities, rendering some nucleation sites inactive, reducing the number of active nucleation sites, and decreasing vapor embryo size. Consequently, two-phase heat transfer performance declines, and the boiling curve shifts to the right. Moreover, with fewer active vapor embryos on the oxidized wall, heat release from the ethylene glycol–water solution is impeded compared with the uncleaned surface, causing persistent fluid superheating. Once the superheat reaches a critical threshold, a large number of nucleation sites are activated simultaneously, generating dense bubbles and leading to periodic explosive boiling. After each explosive boiling event, the fluid requires time to accumulate heat, during which bubbles are smaller and sparser, until the next explosive boiling occurs-completing a cycle of approximately 1.5 ms. This behavior originates from oxidation-induced changes to the liquid–solid interfacial properties, which alter the nucleation process and bubble behavior, thereby modifying the two-phase heat transfer mechanism.

Fig. 13 shows the temporal variation of bubble number for the two surfaces processed using MATLAB. The cleaned surface exhibits a nearly constant bubble count, indicating stable nucleate boiling, whereas the uncleaned surface shows periodic fluctuations, confirming the occurrence of explosive boiling.

3.5. Flow boiling heat transfer in titanium narrow-gap channels at sub-atmospheric pressures

During prolonged boiling experiments, the surface of the TNGC gradually changed from brown-yellow to black, with discoloration occurring at a wall temperature of approximately 180 °C and a heat flux of about 280 W·cm^{-2}. To minimize the potential effects of oxidative decomposition of the ethylene glycol–water solution and oxidation of the channel surface on the experimental results, the maximum heat flux in the TNGC boiling experiments was limited to 250 W·cm^{-2}. Under these conditions, no surface discoloration was observed, and the working fluid was replaced every 2–3 days.

To provide additional reference data and performance analysis for TNGC applications, experiments were conducted under various operating conditions, including mass fluxes of 750, 1500, and 2000 kg·m^{-2}·s^{-1}; inlet subcooling of 35, 25, and 20 °C; and saturation temperatures of 80, 85, and 90 °C. A small number of data points slightly above 250 W·cm^{-2} were collected to complete the boiling-curve trend, but these short-duration measurements remained within a safe thermal window and did not induce surface oxidation or alter the heat-transfer surface characteristics.

3.5.1. Effect of mass flux on heat transfer performance

Fig. 14 shows the boiling curves of the TNGC at three different mass fluxes under an inlet subcooling of 25 °C and a saturation temperature of 90 °C. These curves cover the entire process from the initial single-phase region to conditions below the CHF. At the beginning of the experiment, when the heat flux is low, the flow in

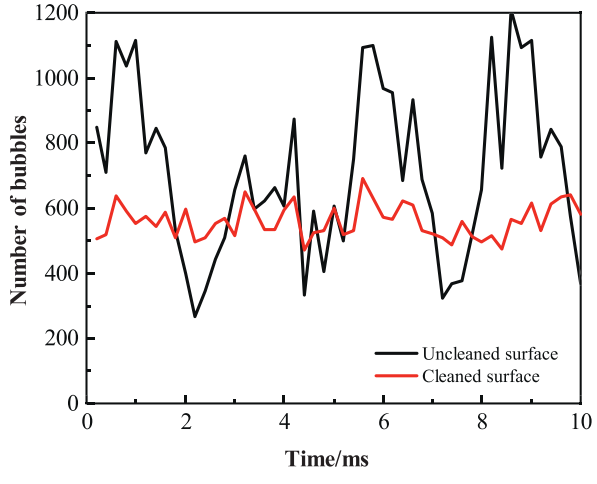


Fig. 13. The number of bubbles varies with time.

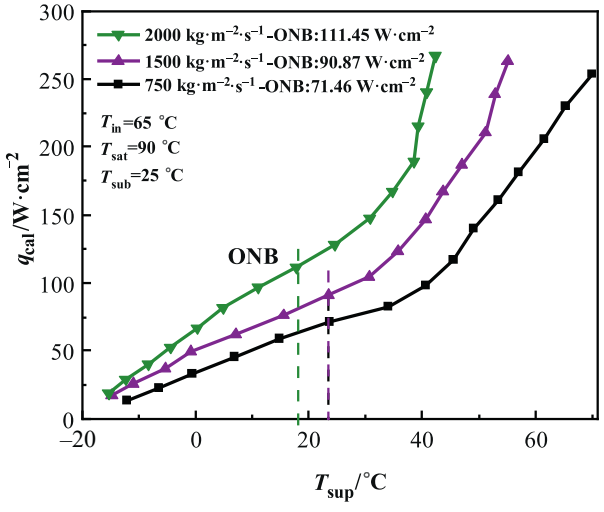


Fig. 14. Boiling curves of TNGC under different mass flow.

the channel is single-phase. As the heat flux increases, the superheat of the ethylene glycol–water solution rises until the ONB occurs. Unlike channels made of copper or aluminum, the boiling curve of the TNGC maintains its initial slope for a period after ONB before increasing significantly at higher heat fluxes. This behavior is attributed to the low thermal conductivity of titanium, which requires higher heat fluxes to sustain more bubble generation.

From an energy balance perspective, more than half of the energy required for bubble growth comes from microlayer evaporation [37]. In the present study, the TNGC has low thermal conductivity and a wall thickness of only 400 μm; lateral heat conduction is negligible, and the heat for microlayer evaporation can only be supplied by the sensible heat from the area of the TNGC in contact with the base of the bubble. At low heat fluxes, this sensible heat is insufficient to support bubble growth to volumes comparable with those in copper narrow-gap channels, resulting in smaller bubble sizes. Immediately after ONB at low heat flux, a limited number of bubbles formed on the wall, causing localized disturbances; however, due to the small bubble population, overall heat transfer remains dominated by single-phase convection, with performance only slightly improved or nearly unchanged. This stage is referred to as the boiling development regime. As the heat flux increases further, more nucleation sites are activated, leading to vigorous boiling and transition into the fully developed boiling regime.

In the single-phase regime, higher mass fluxes yield significantly greater heat transfer capability than lower mass fluxes. The effect of mass flux on heat transfer becomes more pronounced as the heat flux increases. As shown in Fig. 14, higher mass fluxes produce larger surface temperature gradients, requiring higher heat fluxes to initiate ONB. When the mass flux increases from 750 to 2000 $kg \cdot m^{-2} \cdot s^{-1}$, the heat flux required for ONB rises from 71.45 W to 90.87 and 111.46 $W \cdot cm^{-2}$, representing increases of 27.17% and 55.98%, respectively, compared with 750 $kg \cdot m^{-2} \cdot s^{-1}$.

After ONB, the boiling development regime exhibits similar behavior across all mass fluxes, with wall superheat increasing by approximately 17 °C compared to ONB, indicating that mass flux has little influence on the length of this regime. In the fully developed boiling regime, the heat transfer performance at 2000 $kg \cdot m^{-2} \cdot s^{-1}$ is significantly higher than at other mass fluxes. At a wall superheat of 40 °C, the heat flux for 2000 $kg \cdot m^{-2} \cdot s^{-1}$ is 63.49% and 145.08% higher than those for 1500 and 750 $kg \cdot m^{-2} \cdot s^{-1}$, respectively.

Fig. 15 compares the average heat transfer coefficient (h) and the two-phase heat transfer coefficient (h_{tp}) of the TNGC at different mass fluxes. As shown in Fig. 15(a), the h in the single-phase region is not constant but initially increases and then gradually decreases. This behavior can be attributed to the thermophysical properties of the titanium alloy employed.

In the TNGC, higher mass flux results in greater shear forces exerted by the liquid on bubbles, leading to higher bubble departure frequencies and shorter residence times within the channel. This suppresses bubble coalescence and growth, effectively preventing slug flow and associated flow blockages. As a result, the channel can maintain a stable bubbly flow regime with superior heat transfer performance, thereby significantly increasing the heat transfer coefficient. At high mass flux, stronger shear forces not only enhance bubble detachment frequency but also intensify bubble coalescence, detachment, and sliding-induced disturbances to the bulk flow. This promotes enhanced interlayer mixing within the flow, further augmenting the heat transfer coefficient.

Throughout the two-phase boiling region, the h remains stable in the vicinity of ONB and during the boiling development stage, as the characteristics of two-phase heat transfer are not yet prominent—consistent with the titanium boiling results reported by Yin *et al.* [38]. In the fully developed boiling regime, h increases markedly compared with the development stage at the same mass flux, owing to the large-scale generation of bubbles and the dominant contribution of latent heat transport over sensible heat in the ethylene glycol–water mixture. Nevertheless, the enhancement of h between the fully developed and development stages shows a diminishing marginal effect with increasing mass flux: as mass flux rises from 750 to 2000 $kg \cdot m^{-2} \cdot s^{-1}$, the enhancement ratio decreases from 1.66 to 1.30.

To more accurately capture the influence of mass flux on two-phase heat transfer, the h_{tp} is used as a reference. The h_{tp} exhibits a trend of initially decreasing and then increasing with heat flux. In the early stage of nucleate boiling, surface micro/nano structural imperfections act as active nucleation sites, generating small isolated bubbles immediately after ONB. These isolated

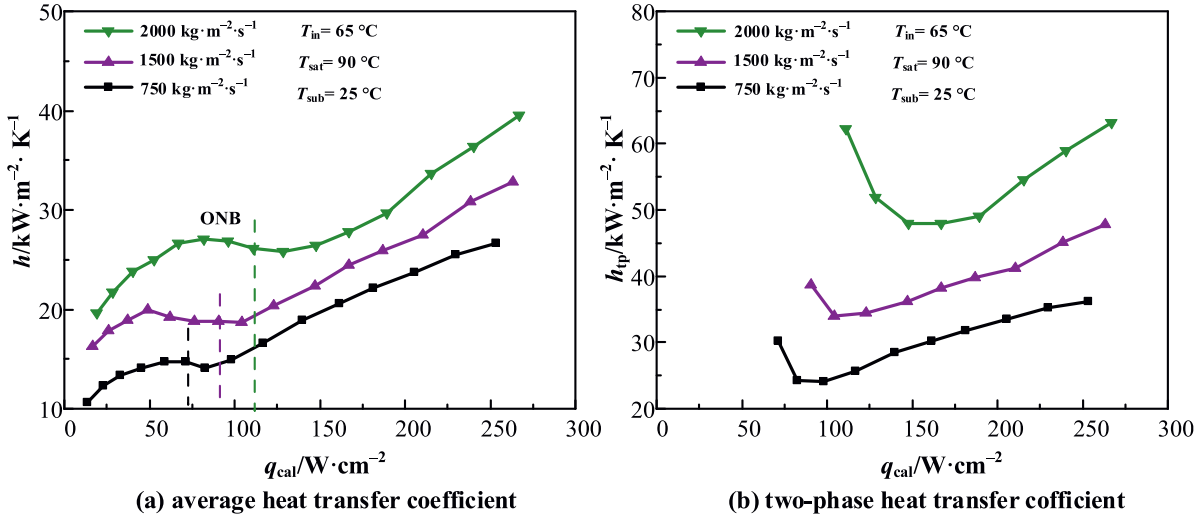


Fig. 15. Heat transfer coefficients of TNGC under different mass flux.

bubbles are quickly swept away by the surrounding subcooled liquid, removing latent heat and inducing flow disturbances, thereby yielding relatively high h_{tp}. As heat flux increases, bubble population grows and bubbles are no longer isolated, leading to a decline in h_{tp}. The higher velocities in the narrow-slit channel reduce bubble departure diameters and increase detachment frequency, suppressing nucleate boiling; this suppression becomes more pronounced with increasing mass flux, resulting in a significant reduction in h_{tp}. When the heat flux increases further, more nucleation sites are activated, producing sufficient bubble populations to promote bubble coalescence [39] and the MEB phenomenon. First, bubble spreading in both upstream and downstream directions enhances microlayer evaporation and thin-film evaporation along the wall, significantly improving boiling heat transfer while reducing wall temperature. Second, the occurrence of MEB provides additional nucleation sites for the downstream heated fluid, thereby further intensifying heat transfer and increasing h_{tp}.

3.5.2. Effect of inlet subcooling on heat transfer performance

Fig. 16 presents the boiling curves of the TNGC at different inlet subcooling under a mass flux of $G = 750\ kg{\cdot}m^{-2}{\cdot}s^{-1}$ and a saturation temperature of $T_{sat} = 90\ °C$. As the inlet subcooling decreases, both the wall superheat and heat flux required for the ONB decrease, resulting in a leftward shift of the ONB point. Specifically, when the inlet subcooling is reduced from 30 °C to 20 °C, the ONB heat flux decreases from 86.70 to 60.09 $W{\cdot}cm^{-2}$, and the wall superheat decreases from 26.11 °C to 14.85 °C. This is because a lower inlet subcooling reduces the sensible heat that must be absorbed by the ethylene glycol–water solution before boiling initiates, thereby lowering the energy requirement and the corresponding heat flux for ONB.

In the fully developed boiling regime, the boiling curves at subcooling of 30 °C and 25 °C exhibit only minor differences, and both show significantly lower heat transfer performance compared with the 20 °C subcooling condition. At a wall superheat of 35 °C, the heat flux at 20 °C subcooling reaches 193.56 $W{\cdot}cm^{-2}$, which is 93.89% and 133.65% higher than those at 25 °C (99.83 $W{\cdot}cm^{-2}$) and 30 °C (82.84 $W{\cdot}cm^{-2}$), respectively. This indicates that, at higher inlet subcooling, the TNGC heat transfer performance is relatively insensitive to changes in subcooling.

The superior performance at 20 °C subcooling can be attributed to two factors: (1) the reduced energy requirement for boiling initiation in the ethylene glycol–water solution, which promotes more vigorous boiling, greater heat removal, and enhanced turbulence due to the detachment of a larger number of bubbles; and (2) the low thermal conductivity and small wall thickness (low thermal mass) of the TNGC, which limit the energy available for bubble growth. At inlet subcooling of 25 °C and 30 °C, bubbles generated in the ethylene glycol–water solution are smaller and fewer, resulting in weaker heat transfer enhancement.

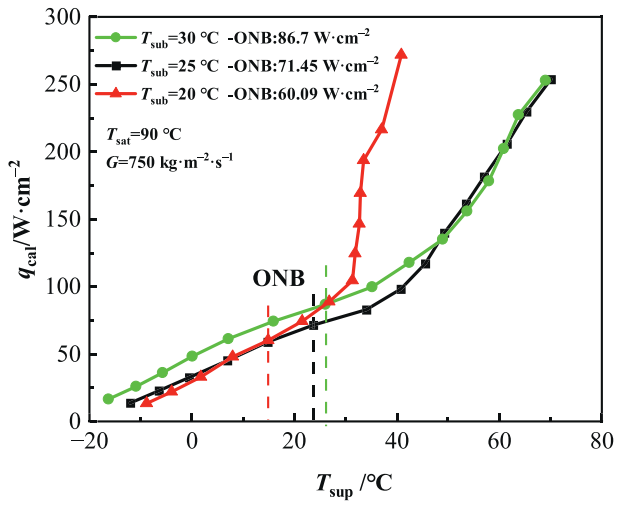


Fig. 16. Boiling curves of TNGC under different inlet subcooling temperatures.

Fig. 17 illustrates the variation of the h and the h_{tp} with heat flux under different inlet subcooling conditions. Following the ONB, the h for the 20 °C subcooling condition exhibits a rapid increase within a relatively small heat flux range, requiring a much smaller heat flux increment compared to the 30 °C and 25 °C subcooling cases. In the fully developed boiling regime, a lower subcooling and correspondingly higher inlet temperature reduce the energy required for the ethylene glycol–water solution to reach the boiling state, thereby promoting more vigorous boiling, greater bubble generation, and consequently higher h. At a mass flux of 750 $kg{\cdot}m^{-2}{\cdot}s^{-1}$, the fully developed boiling h at 20 °C subcooling is approximately 65% higher than those at 30 °C and 25 °C subcooling, while the values for inlet temperatures of 60 °C and 65 °C are nearly identical. This further confirms that, at relatively high subcooling, the TNGC exhibits limited sensitivity to subcooling variations. From a practical standpoint, considering pump power consumption and the temperature dependence of the ethylene glycol–water solution viscosity, a smaller subcooling is more favorable for operational efficiency.

The h_{tp} exhibits a characteristic trend of initially decreasing and then increasing. The heat flux range corresponding to the decreasing segment is nearly identical across all three subcooling conditions, corroborating the earlier explanation that the reduction in h_{tp} arises from the suppressive effect of fluid velocity on nucleate boiling. Furthermore, Fig. 17 clearly shows that, at higher heat fluxes, the h_{tp} curves for the 30 °C and 25 °C subcooling conditions almost completely overlap, indicating essentially identical two-phase heat transfer performance and reinforcing the conclusion that, at higher subcooling, the TNGC is insensitive to subcooling changes.

Under the baseline condition (inlet subcooling of 25 °C and mass flux of 750 $kg{\cdot}m^{-2}{\cdot}s^{-1}$), both reducing the inlet subcooling to 20 °C and increasing the mass flux to 2000 $kg{\cdot}m^{-2}{\cdot}s^{-1}$ yield comparable enhancements in heat transfer performance, lowering the channel bottom temperature by approximately 6.5%. In practical applications, the optimal strategy for enhancing heat transfer must account for both pressure drop and pump power requirements.

Analysis of the data in Fig. 18 shows that reducing the inlet subcooling to 20 °C results in a negligible pressure drop of only 0.5 kPa. In contrast, increasing the mass flux to 2000 $kg{\cdot}m^{-2}{\cdot}s^{-1}$ leads to a substantial increase in pressure drop, reaching 3 kPa. Therefore, from a system-level perspective, lowering the inlet temperature is a more favorable approach than increasing mass flux, primarily due to its minimal impact on system pressure losses.

3.5.3. Effect of saturation temperature on heat transfer performance

Fig. 19 illustrates the boiling curves of the TNGC under different saturation pressures (saturation temperatures), with the corresponding saturation pressures listed in Table 4. In the single-phase heat transfer regime, the three curves nearly overlap, as identical inlet temperatures result in negligible variation in fluid thermophysical properties-such as viscosity and Prandtl number-consistent with single-phase heat transfer theory.

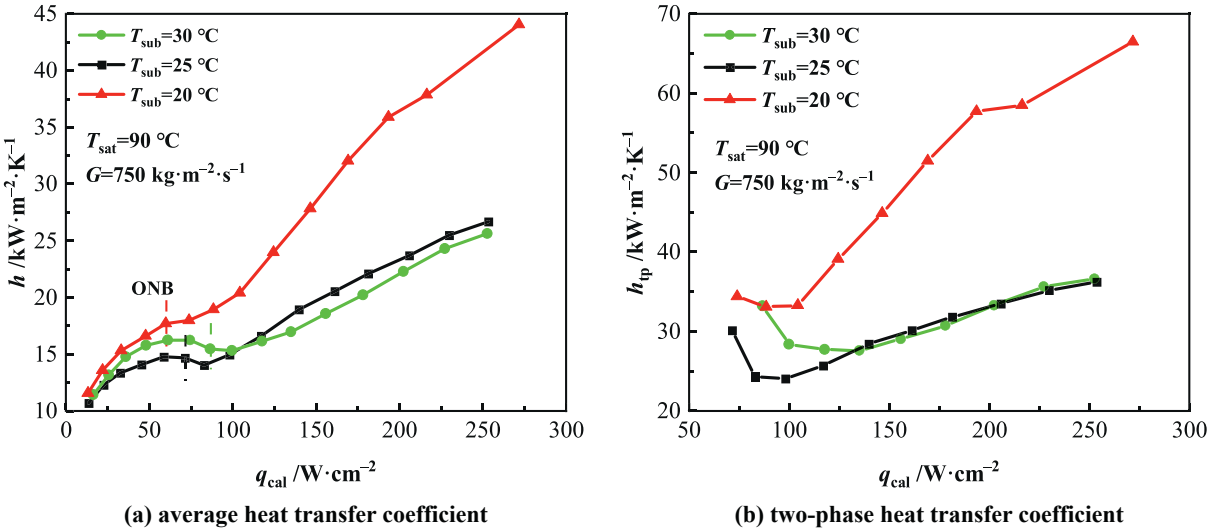


Fig. 17. Heat transfer coefficients of TNGC under int inlet subcooling temperatures differed.

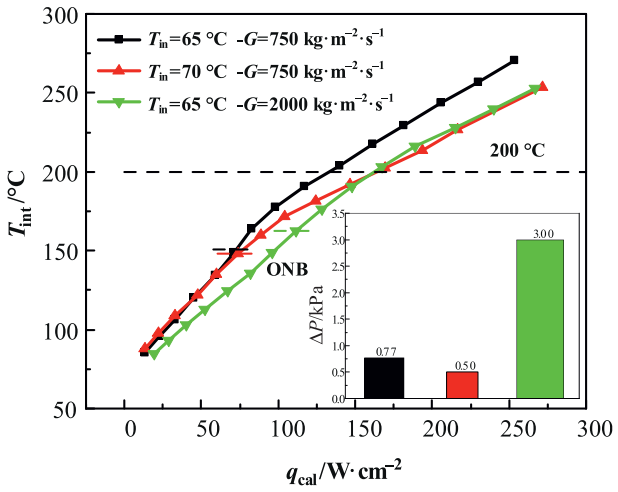


Fig. 18. Relationship between pressure drop and mass flux.

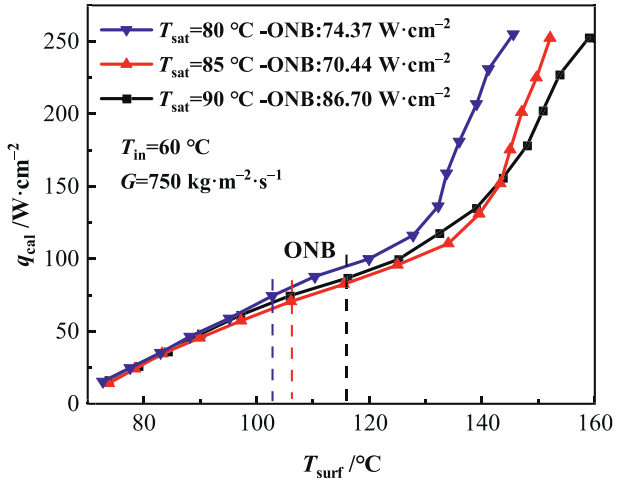


Fig. 19. Boiling curves of TNGC under different pressures.

Table 4
Saturation temperature of ethylene glycol aqueous solution under different saturation.

Saturation pressures/kPa	Saturation temperature T_{sat}/°C
35.2 ± 0.5	80 ± 0.35
42.9 ± 0.5	85 ± 0.3
51.9 ± 0.5	90 ± 0.3

The influence of saturation temperature on TNGC performance becomes evident in the two-phase region. A lower saturation temperature corresponds to a reduced system saturation pressure, meaning that under identical inlet temperature conditions, the sensible heat required for the ethylene glycol–water mixture to reach boiling is lower, thereby reducing the heat flux at the ONB. As shown in Fig. 19, the heat flux required for ONB at saturation temperatures of 80 °C is 12.34 W·cm^{-2} lower than that at 90 °C.

Furthermore, a lower saturation pressure decreases the resistance to bubble departure, increasing the bubble departure frequency. According to Carey's theory [40], the departure frequency is inversely proportional to the departure diameter. Consequently, while a higher departure frequency and smaller bubble size may not necessarily increase the total heat removed by bubbles, notable differences in the boiling curves are observed across the three back-pressure conditions.

Fig. 20 presents the variation of the h and the h_{tp} for the TNGC under different saturation temperatures. Overall, in the fully developed boiling regime, the h increases markedly with decreasing saturation temperature. This trend is directly associated with the reduction in saturation pressure, which facilitates bubble growth and detachment, and increases bubble departure frequency. Specifically, h at a saturation temperature of 80 °C is 9.6% higher than at 85 °C, while at 85 °C it is 6.1% higher than at 90 °C. For the h_{tp}, although numerical differences are observed across the three saturation temperature conditions, the variations are relatively small. Compared with other methods of enhancing boiling heat transfer performance, adjusting the saturation temperature has a comparatively limited influence on both h and h_{tp}.

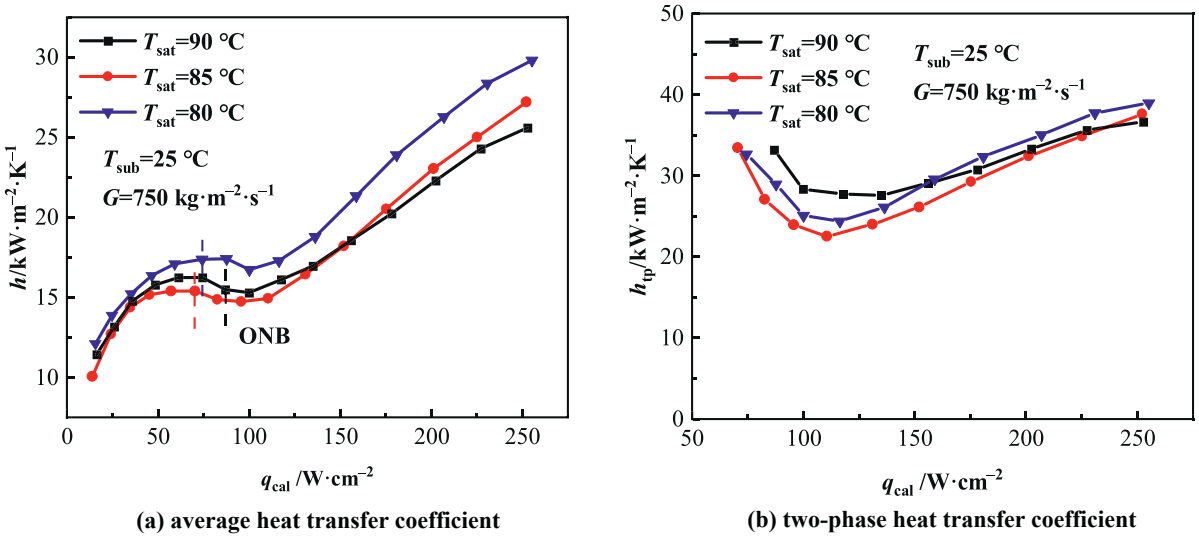


Fig. 20. Heat transfer coefficients of TNGC under different saturation pressures.

4. Conclusions

To comprehensively investigate the heat transfer performance of a TNGC using an ethylene glycol–water solution as the working fluid under sub-atmospheric pressure, and to provide both data support and theoretical insights for practical engineering applications, a series of experiments were conducted. The tests systematically considered a range of operating parameters, including mass fluxes of 750, 1500, and 2000 kg·m^{-2}·s^{-1}, inlet subcooling of 35, 25, and 20 °C, and saturation temperatures of 80, 85, and 90 °C. The influence of these parameters on the boiling curves, heat transfer coefficients, and base surface temperature was analyzed in detail. In addition, the preparation procedures for the preliminary tests are described. The main conclusions of this study are summarized as follows:

(1) Compared with deionized water, the ethylene glycol–water solution exhibits higher viscosity, lower thermal conductivity, and stronger temperature dependence, resulting in a heat transfer performance that is approximately 60% of that of water under identical conditions. Channel height has a pronounced effect: the 1 mm and 0.5 mm channels outperform the 2 mm channel, while the 0.5 mm channel incurs a substantially higher pressure drop. Thus, a 1 mm channel height provides the optimal balance between heat transfer and hydraulic performance.

(2) Flow in the TNGC is characterized by bubbly flow and slug flow, with MEB occurring at higher heat fluxes. Surface oxidation induces a transition from stable nucleate boiling to periodic explosive boiling, causing severe degradation of heat transfer performance. Acidification and thermal decomposition of the ethylene glycol–water solution further reduce boiling effectiveness. Although oxidation cannot be fully eliminated, its impact was reduced by limiting surface temperature and replacing the working fluid every 2–3 days.

(3) Increasing mass flux significantly improves both h and h_{tp}, but the enhancement of nucleate boiling diminishes, as reflected by the reduction of the nucleate boiling enhancement factor from 1.66 to 1.30 as mass flux increases. Lowering saturation temperature slightly increases bubble departure frequency and promotes earlier phase change, but the improvement in heat transfer coefficient is relatively modest compared with mass flux and subcooling effects.

(4) At large subcooling levels, boiling curves nearly overlap, indicating minimal influence on two-phase heat transfer. At lower subcooling, reducing the subcooling produces substantial enhancement: the average heat transfer coefficient increases by approximately 65% when inlet subcooling is reduced from 30 °C to 20 °C. Considering both thermal performance and pressure-drop penalties, lowering subcooling is generally more practical for engineering implementation than increasing mass flux.

CRediT Authorship Contribution Statement

Dahai Wang: Writing – review & editing, Writing – original draft, Visualization, Validation, Software, Methodology, Data curation, Conceptualization. Xianan Yin: Writing – review & editing, Writing – original draft, Validation, Software. Chen Zhao: Validation, Methodology, Investigation, Conceptualization. Qiushi Gu: Writing – original draft, Software, Data curation, Conceptualization. Chaoyang Zhang: Writing – review & editing, Writing – original draft, Visualization, Supervision, Software, Resources, Funding acquisition, Data curation.

Declaration of Competing Interest

The authors declare that they have no known competing financial interests or personal relationships that could have appeared to influence the work reported in this paper.

Acknowledgements

This work is sponsored by the National Natural Science Foundation of China (52506063, 52306262) and the Scientific Research Foundation for High-level Talents of Anhui University of Science and Technology (2024yjrc84).

References

[1] M.A. Ebadian, C.X. Lin, A review of high-heat-flux heat removal technologies, *J. Heat Tran.* 133 (11) (2011) 110801.

[2] R. van Erp, R. Soleimanzadeh, L. Nela, G. Kampitsis, E. Matioli, Co-designing electronics with microfluidics for more sustainable cooling, *Nature* 585 (7824) (2020) 211–216.
[3] L.X. Yang, A. Guo, W. Zhang, Computational fluid dynamics simulation of subcooled flow boiling in vertical rectangular 2-mm narrow channel, *Adv. Mech. Eng.* 7 (7) (2015) 1–12.
[4] K. Zhou, C. Coyle, J.Y. Li, J. Buongiorno, W. Li, Flow boiling in vertical narrow microchannels of different surface wettability characteristics, *Int. J. Heat Mass Tran.* 109 (2017) 103–114.
[5] R.A. Krishnan, K.R. Balasubramanian, S. Suresh, Experimental investigation of the effect of heat sink orientation on subcooled flow boiling performance in a rectangular microgap channel, *Int. J. Heat Mass Tran.* 120 (2018) 1341–1357.
[6] T. Alam, P.S. Lee, C.R. Yap, L.W. Jin, A comparative study of flow boiling heat transfer and pressure drop characteristics in microgap and microchannel heat sink and an evaluation of microgap heat sink for hotspot mitigation, *Int. J. Heat Mass Tran.* 58 (1–2) (2013) 335–347.
[7] W.H. Yu, D.M. France, D. Singh, W.H. Zhao, Experimental investigation of subcooled flow boiling of a 50/50 ethylene glycol/water mixture in finned rectangular aluminum channels, *Exp. Heat Transf.* 31 (6) (2018) 482–494.
[8] X.Y. Hu, Y. Wang, S.Y. Li, Q. Sun, G.X. Li, S.Z. Bai, K. Sun, Investigation on subcooled flow boiling heat transfer characteristics in ICE-like conditions, *Open Phys.* 19 (1) (2021) 413–425.
[9] W. Yu, D.M. France, W. Zhao, D. Singh, R.K. Smith, Subcooled flow boiling heat transfer to water and ethylene glycol/water mixtures in a bottom-heated tube, *Exp. Heat Transf.* 29 (5) (2016) 593–614.
[10] J. Lee, L.E. O'Neill, S. Lee, I. Mudawar, Experimental and computational investigation on two-phase flow and heat transfer of highly subcooled flow boiling in vertical upflow, *Int. J. Heat Mass Tran.* 136 (2019) 1199–1216.
[11] Z. Liu, R.H.S. Winterton, A general correlation for saturated and subcooled flow boiling in tubes and annuli, based on a nucleate pool boiling equation, *Int. J. Heat Mass Tran.* 34 (11) (1991) 2759–2766.
[12] A.S. Pamitran, K.I. Choi, J.T. Oh, P. Hrnjak, Characteristics of two-phase flow pattern transitions and pressure drop of five refrigerants in horizontal circular small tubes, *Int. J. Refrig.* 33 (3) (2010) 578–588.
[13] K. Wojtasik, R. Rullière, Z. Krolicki, B. Zajaczkowski, J. Bonjour, Subcooled boiling regime map for water at low saturation temperature and subatmospheric pressure, *Exp. Therm. Fluid Sci.* 118 (2020) 110150.
[14] P.K. Das, S. Chakraborty, S. Bhaduri, Critical heat flux during flow boiling in mini and microchannel—a state of the art review, *Front. Heat Mass Tran.* 3 (1) (2012) 013008.
[15] N. Colgan, J.L. Bottini, R. Martínez-Cuenca, C.S. Brooks, Experimental study of critical heat flux in flow boiling under subatmospheric pressure in a vertical square channel, *Int. J. Heat Mass Tran.* 130 (2019) 514–522.
[16] C.P. Yin, Y.Y. Yan, T.F. Lin, B.C. Yang, Subcooled flow boiling heat transfer of R-134a and bubble characteristics in a horizontal annular duct, *Int. J. Heat Mass Tran.* 43 (11) (2000) 1885–1896.
[17] W.R. Chang, C.A. Chen, J.H. Ke, T.F. Lin, Subcooled flow boiling heat transfer and associated bubble characteristics of FC-72 on a heated micro-pin-finned silicon chip, *Int. J. Heat Mass Tran.* 53 (23–24) (2010) 5605–5621.
[18] J. Wang, K.H. Lu, S. Lu, H.J. Zhang, Experimental study on ceiling temperature profile of sidewall fires at reduced pressure in an aircraft cargo compartment, *Exp. Therm. Fluid Sci.* 82 (2017) 326–332.
[19] Z. Rahimi-Ahar, M.S. Hatamipour, Y. Ghalavand, A. Palizvan, Comprehensive study on vacuum humidification–dehumidification (VHDH) desalination, *Appl. Therm. Eng.* 169 (2020) 114944.
[20] Z.Q. Xiong, C. Ye, M.L. Wang, H.Y. Gu, Experimental study on the sub-atmospheric loop heat pipe passive cooling system for spent fuel pool, *Prog. Nucl. Energy* 79 (2015) 40–47.
[21] S.M. Peyghambarzadeh, S.H. Hashemabadi, S.M. Hoseini, M. Seifi Jamnani, Experimental study of heat transfer enhancement using water/ethylene glycol based nanofluids as a new coolant for car radiators, *Int. Commun. Heat Mass Tran.* 38 (9) (2011) 1283–1290.
[22] C. Selvam, E.C. Muhammed Irshad, D.M. Lal, S. Harish, Convective heat transfer characteristics of water–ethylene glycol mixture with silver nanoparticles, *Exp. Therm. Fluid Sci.* 77 (2016) 188–196.
[23] W.H. Azmi, K.A. Hamid, N.A. Usri, R. Mamat, K.V. Sharma, Heat transfer augmentation of ethylene glycol: water nanofluids and applications: a review, *Int. Commun. Heat Mass Tran.* 75 (2016) 13–23.
[24] L.S. Sundar, M.K. Singh, A.C.M. Sousa, Thermal conductivity of ethylene glycol and water mixture based Fe_3O_4 nanofluid, *Int. Commun. Heat Mass Tran.* 49 (2013) 17–24.
[25] R.J. Moffat, Describing the uncertainties in experimental results, *Exp. Therm. Fluid Sci.* 1 (1) (1988) 3–17.
[26] P.H. Lin, B.R. Fu, C. Pan, Critical heat flux on flow boiling of methanol–water mixtures in a diverging microchannel with artificial cavities, *Int. J. Heat Mass Tran.* 54 (15–16) (2011) 3156–3166.
[27] M.C. Vlachou, J.S. Lioumbas, K. David, D. Chasapis, T.D. Karapantsios, Effect of channel height and mass flux on highly subcooled horizontal flow boiling, *Exp. Therm. Fluid Sci.* 83 (2017) 157–168.
[28] T. Alam, P.S. Lee, C.R. Yap, L.W. Jin, Experimental investigation of local flow boiling heat transfer and pressure drop characteristics in microgap channel, *Int. J. Multiphas. Flow* 42 (2012) 164–174.
[29] M. Lee, L.S.L. Cheung, Y.K. Lee, Y. Zohar, Height effect on nucleation-site activity and size-dependent bubble dynamics in microchannel convective boiling, *J. Micromech. Microeng.* 15 (11) (2005) 2121–2129.
[30] T.C. Willingham, I. Mudawar, Channel height effects on forced-convection boiling and critical heat flux from a linear array of discrete heat sources, *Int. J. Heat Mass Tran.* 35 (8) (1992) 1865–1880.
[31] J.H. Seong, C. Wang, B. Phillips, M. Bucci, Separate effect of oxidation on the subcooled flow boiling performance of Zircaloy-4 at atmospheric pressure, *Int. J. Heat Mass Tran.* 188 (2022) 122620.
[32] P. Jayaramu, S. Gedupudi, S.K. Das, An experimental investigation on the influence of copper ageing on flow boiling in a copper microchannel, *Heat Transf. Eng.* 41 (4) (2020) 333–350.
[33] R.L. Ramakrishnan, P. Jayaramu, S. Gedupudi, S.K. Das, Experimental investigation of the influence of boiling-induced ageing on high heat flux flow boiling in a copper microchannel, *Int. J. Heat Mass Tran.* 181 (2021) 121862.
[34] K. Wang, N. Erkan, K. Okamoto, A study on the effect of oxidation on critical heat flux in flow boiling with downward-faced carbon steel, *Int. J. Heat Mass Tran.* 147 (2020) 118966.
[35] C.H. Wang, V.K. Dhir, Effect of surface wettability on active nucleation site density during pool boiling of water on a vertical surface, *J. Heat Tran.* 115 (3) (1993) 659–669.
[36] F.W. Young, J.V. Cathcart, A.T. Gwathmey, The rates of oxidation of several faces of a single crystal of copper as determined with elliptically polarized light, *Acta Metall.* 4 (2) (1956) 145–152.
[37] E. Lakew, A. Sarchami, G. Giustini, H. Kim, K. Bellur, Thin film evaporation modeling of the liquid microlayer region in a dewetting water bubble, *Fluid* 8 (4) (2023) 126.
[38] L.F. Yin, A. Chauhan, A. Recinella, L. Jia, S.G. Kandlikar, Subcooled flow boiling in an expanding microgap with a hybrid microstructured surface, *Int. J. Heat Mass Tran.* 151 (2020) 119379.
[39] H.T. Phan, N. Caney, P. Marty, S. Colasson, J. Gavillet, Flow boiling of water on nanocoated surfaces in a microchannel, *J. Heat Tran.* 134 (2) (2012) 020901.
[40] V.P. Carey, Liquid–Vapor Phase-Change Phenomena: an Introduction to the Thermophysics of Vaporization and Condensation Processes in Heat Transfer Equipment, third ed., CRC Press, Boca Raton (2020).